EGH404: Fluid Dynamics

COMPUTATIONAL FLUID DYNAMICS REPORT

Group 14

Name	Student Number	Contribution	Signature
Porrel Samana	n10990348	50%	P.S
Ellie Tun	n11309270	50%	H.T.T

Contents

1   PART 1: RESULTS AND DISCUSSION

1.1 GEOMETRY IN DESIGNMODELER [1 Mark]

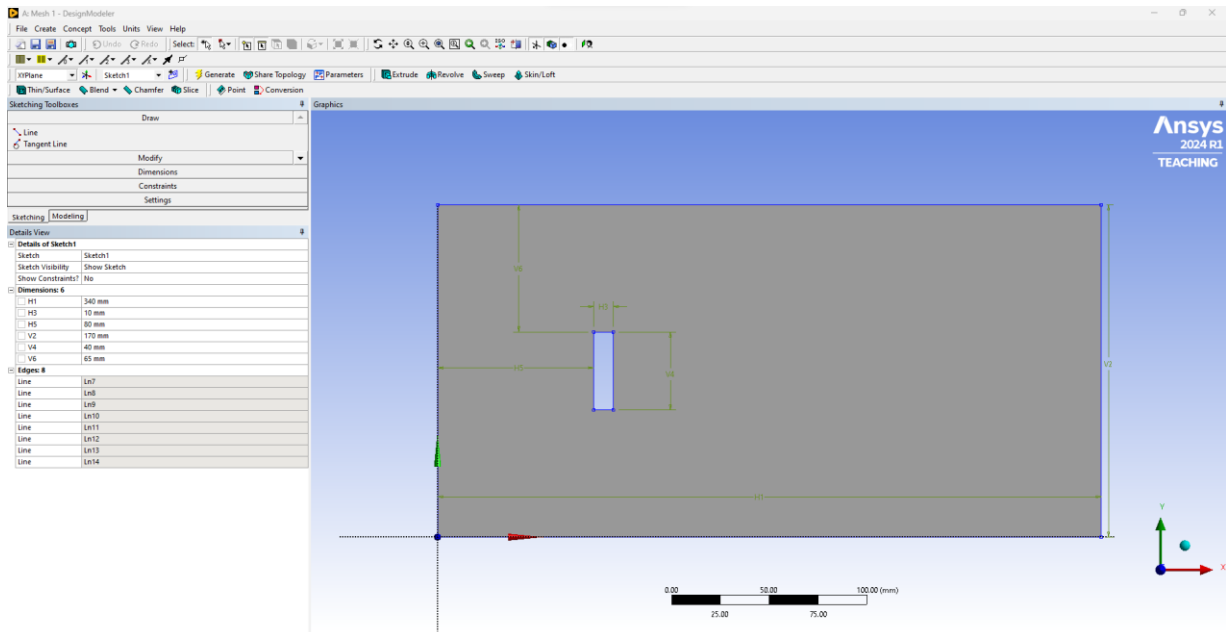
Figure 1.1(i): Geometry Design in ANSYS Fluent DesignModeler

1.2 MESH GENERATION TYPE & REFINEMENT STUDY JUSTIFICATION [2 Marks]

1.   Mesh Generation Type: Normal Triangular Mesh

For this mesh refinement study, a normal triangular mesh was selected due to its suitability for the relatively simple geometry of the body being analysed in this report. The normal mesh type was chosen over the cross-flow mesh due to its ease of implementation and ability to conform to the geometry without excessive complexity. After constructing and examining four normal and cross-flow meshes, (see Figure 1.2(i) for comparison images) the normal meshes proved to be straightforward to interpret and understand. This clarity supported their selection to ensure a well-informed analysis in this report. Additionally, to ensure mesh quality, the measures of smoothness and aspect ratio were prioritized. Initial comparisons between triangular and quadrilateral geometries, conducted after constructing the first two meshes, revealed that the triangular method offered a smoother mesh with an acceptable aspect ratio between cells. Figure 1.1(ii) highlights the superior smoothness and balanced aspect ratio achieved with the triangular geometry, which justified its selection over its quadrilateral counterpart.

2.   Refinement Strategy: Increasing Mesh Resolution and Quality

The refinement strategy involved progressive enhancement of mesh resolution and quality by decreasing element size and increasing the total number of elements by a factor of 1.5 for each successive mesh. To ensure consistency in refinement steps, the scaling factor of 1.5 was chosen as a midpoint within the specified range (1-2). Gradually enhancing mesh resolution and quality allowed for an efficient convergence analysis and thus was selected as the refinement strategy for this report.
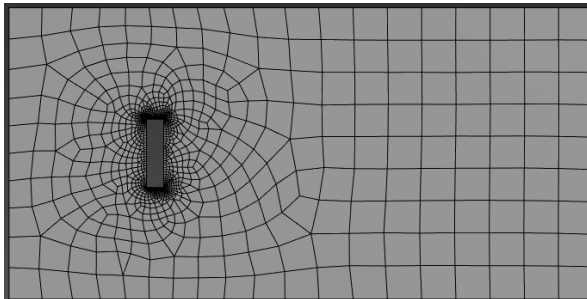
Triangular Geometry
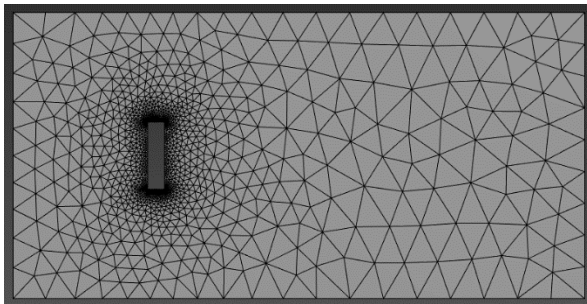
Mesh 1   Mesh 2
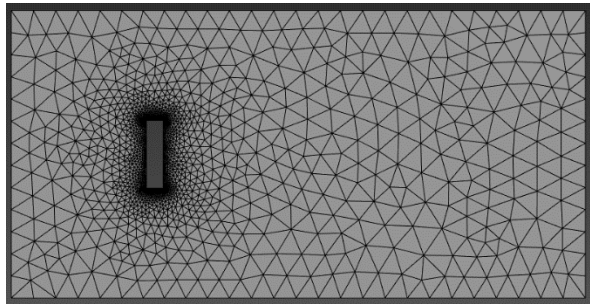
Quadrilateral Geometry

Mesh 1   Mesh 2

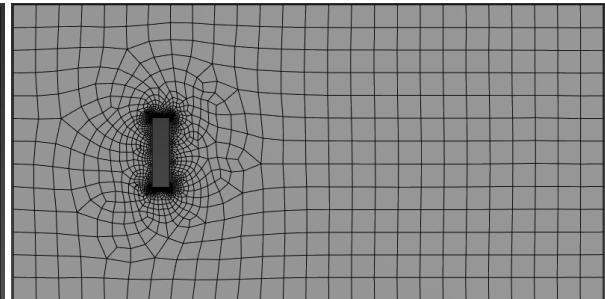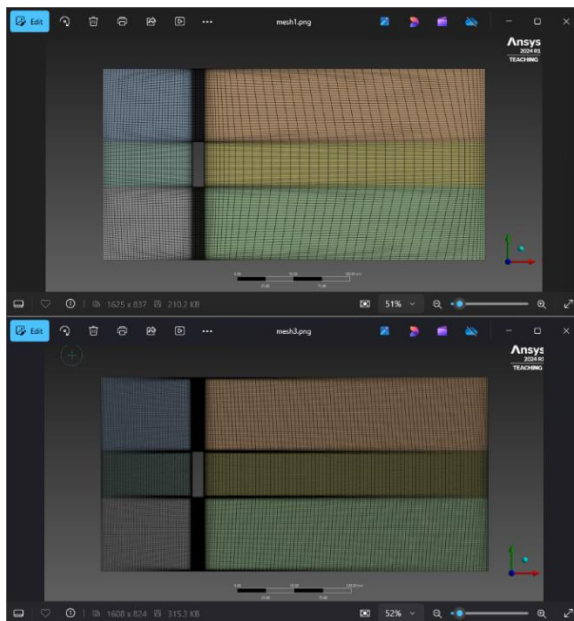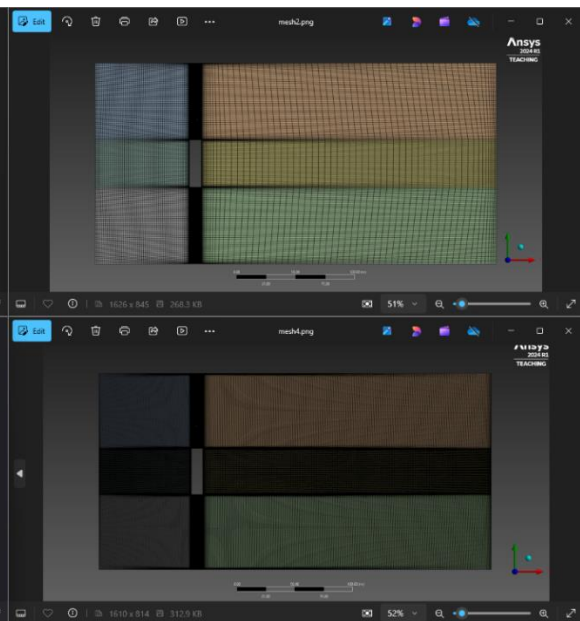Figure 1.1(ii): Triangular vs Quadrilateral Geometry Methods
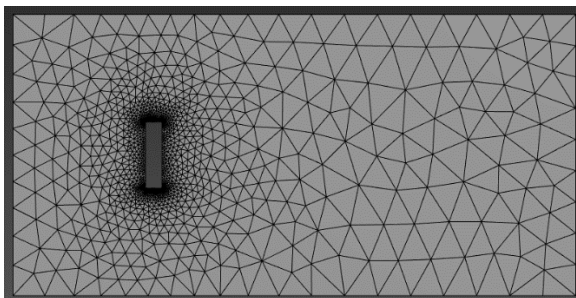
Cross-flow Mesh

Mesh 1   Mesh 2

Mesh 3   Mesh 4
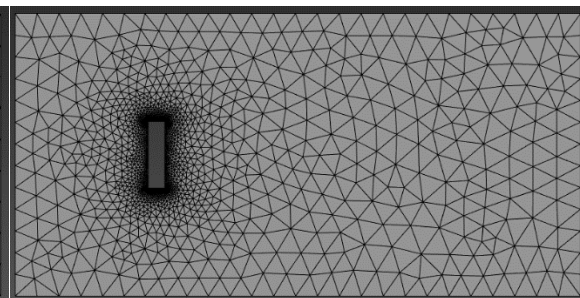
Normal Mesh

Mesh 1   Mesh 2
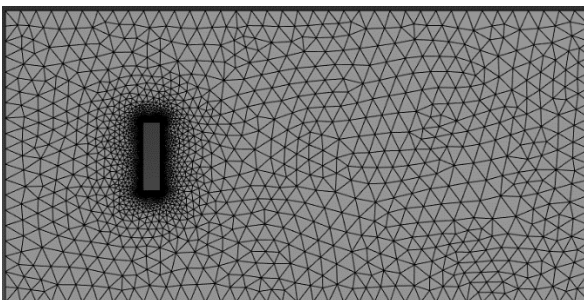
Mesh 3   Mesh 3

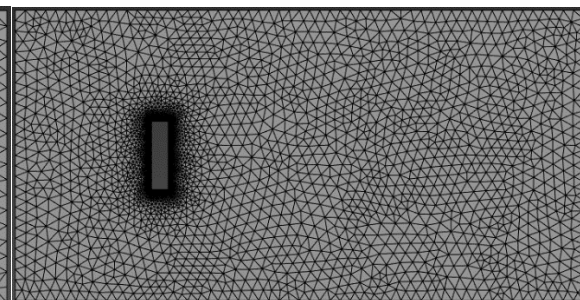Figure 1.2(i): Cross-flow Mesh vs Normal Mesh

1.3 MESH REFINEMENT STUDY: 5 MESH SIZES

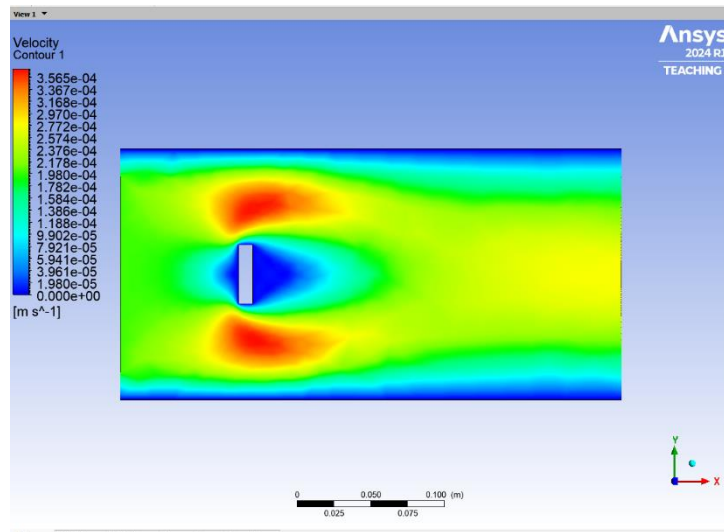### 1.3.1   Velocity Contour Plots [1.5 Marks]

Figure 1.3.1(i): Velocity Contour for Mesh Design 1
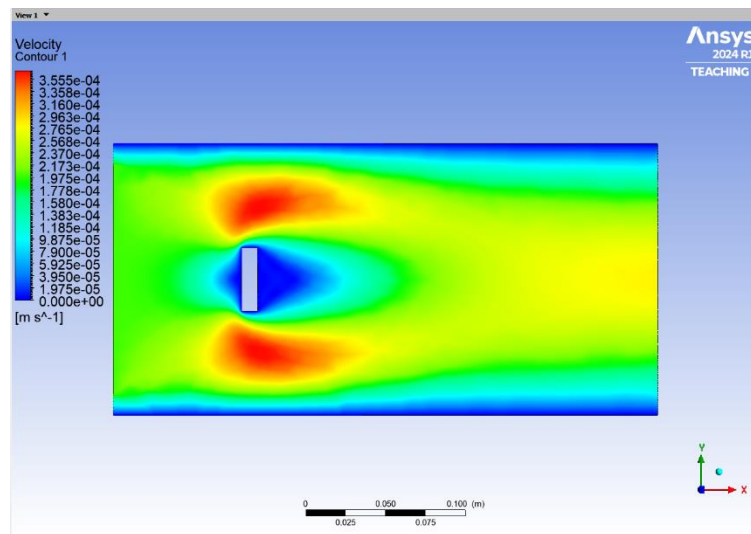
Figure 1.3.1(ii): Velocity Contour for Mesh Design 2
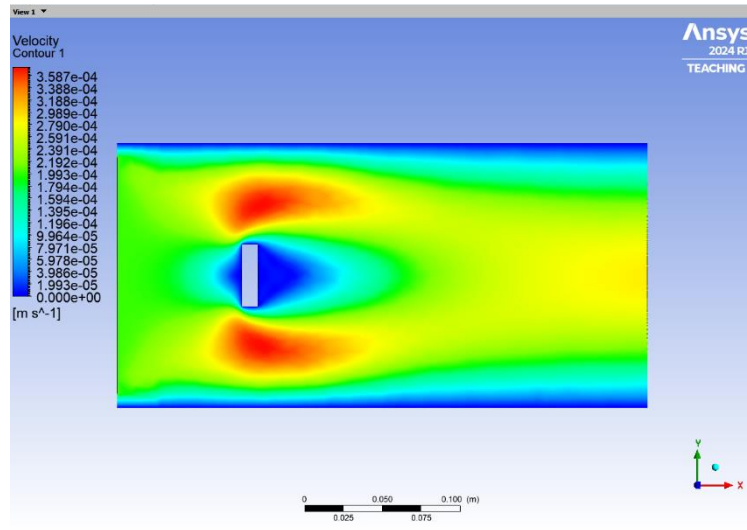
Figure 1.3.1(iii): Velocity Contour for Mesh Design 3
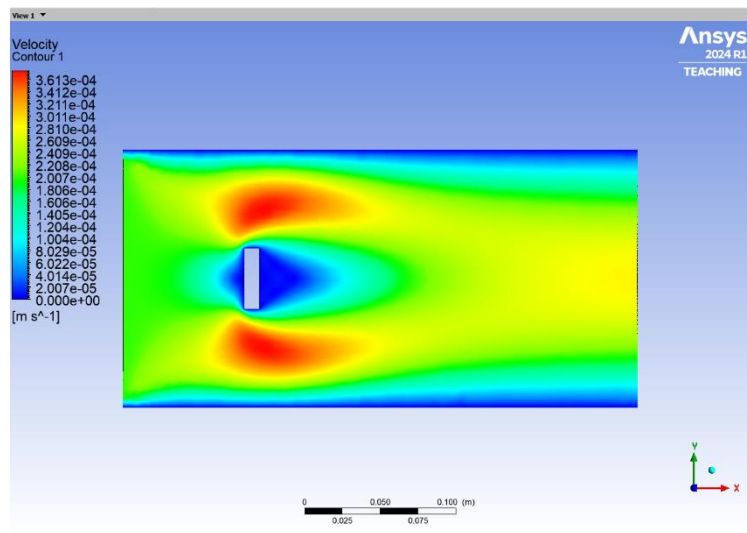
Figure 1.3.1(iv): Velocity Contour for Mesh Design 4
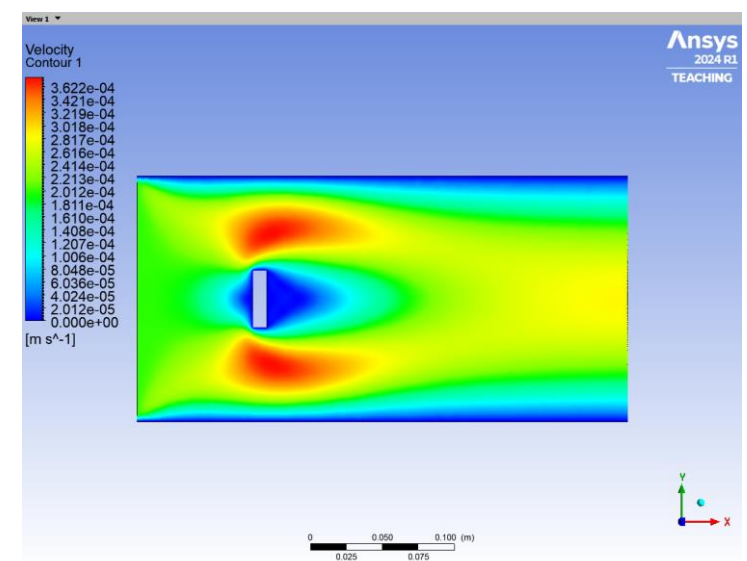
Figure 1.3.1(v): Velocity Contour for Mesh Design 5

1.3.2   Velocity Profiles at Line A & Line B [1.5 Marks]

Velocity Profiles at Line A and B
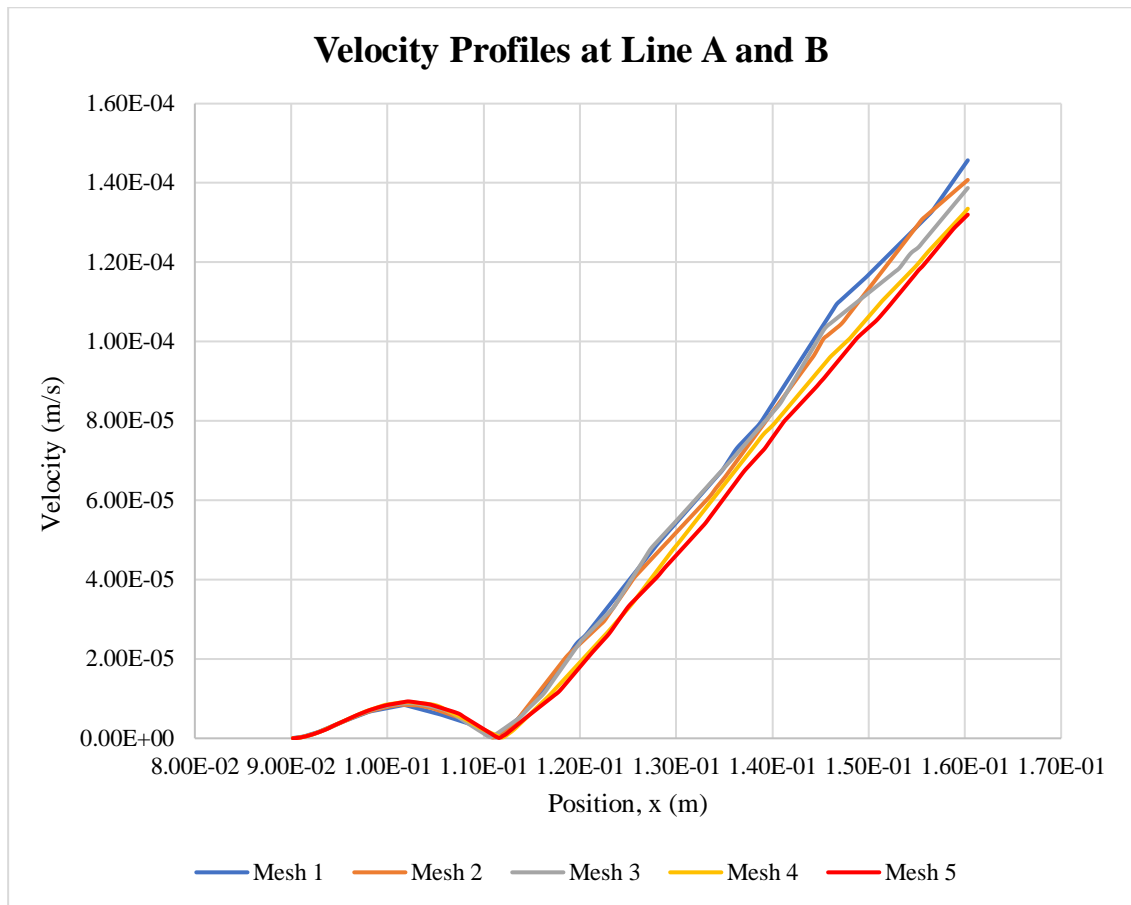
Figure 1.3.2(i): Plot for Velocity Profiles at Line A & Line B for all four Mesh Designs

1.3.3   Table of Values & Graph of Drag Coefficient vs. Number of Elements [1.5 Marks]

Mesh	No. of Elements 2	Drag Coefficient
1	2799	8.3876
2	4212	8.4568
3	6334	8.5107
4	10580	8.5591
5	18700	8.5746

Table 1.3.3(i): Table of Drag Coefficient and Number of Elements for each Mesh.

Figure 1.3.3(i): Plot for Drag Coefficient vs. Number of Elements

1.3.4   Formation Length

Mesh #	Formation Length (m)
Mesh 1	0.111631826
Mesh 2	0.111291483
Mesh 3	0.110951141
Mesh 4	0.112312511
Mesh 5	0.111972168

Table 1.3.4(i): Table of Formation Lengths for each Mesh.

Figure 1.3.4(i): Velocity Profiles for each Mesh

1.4 DISCUSSION [4 Marks]

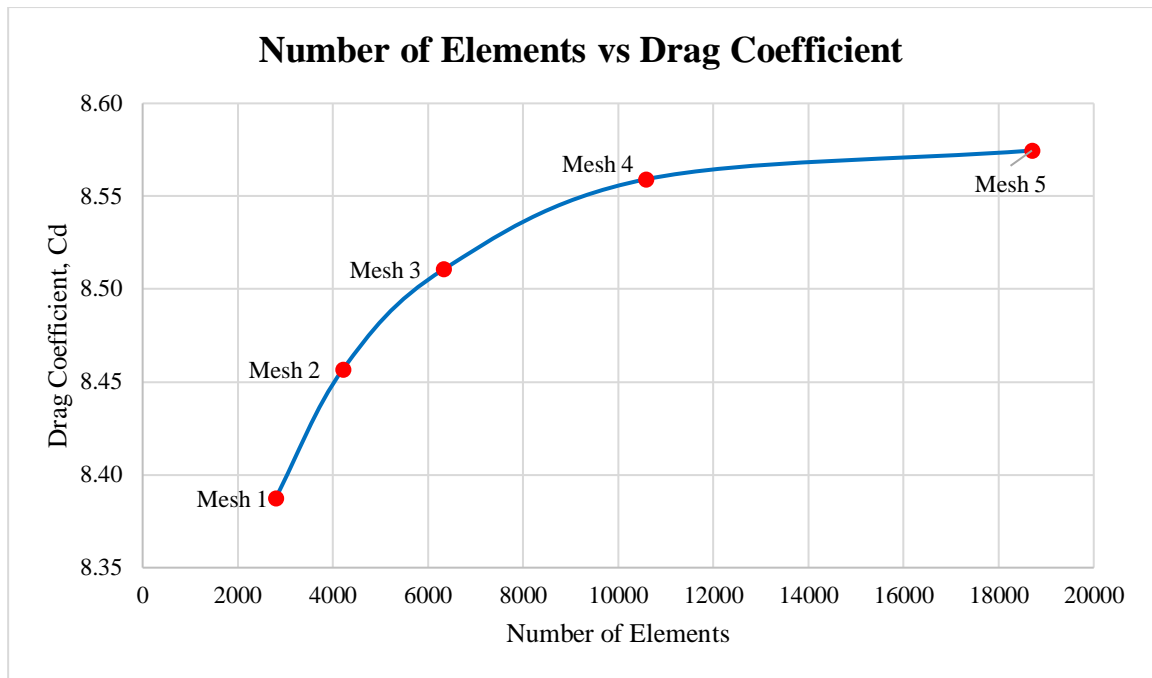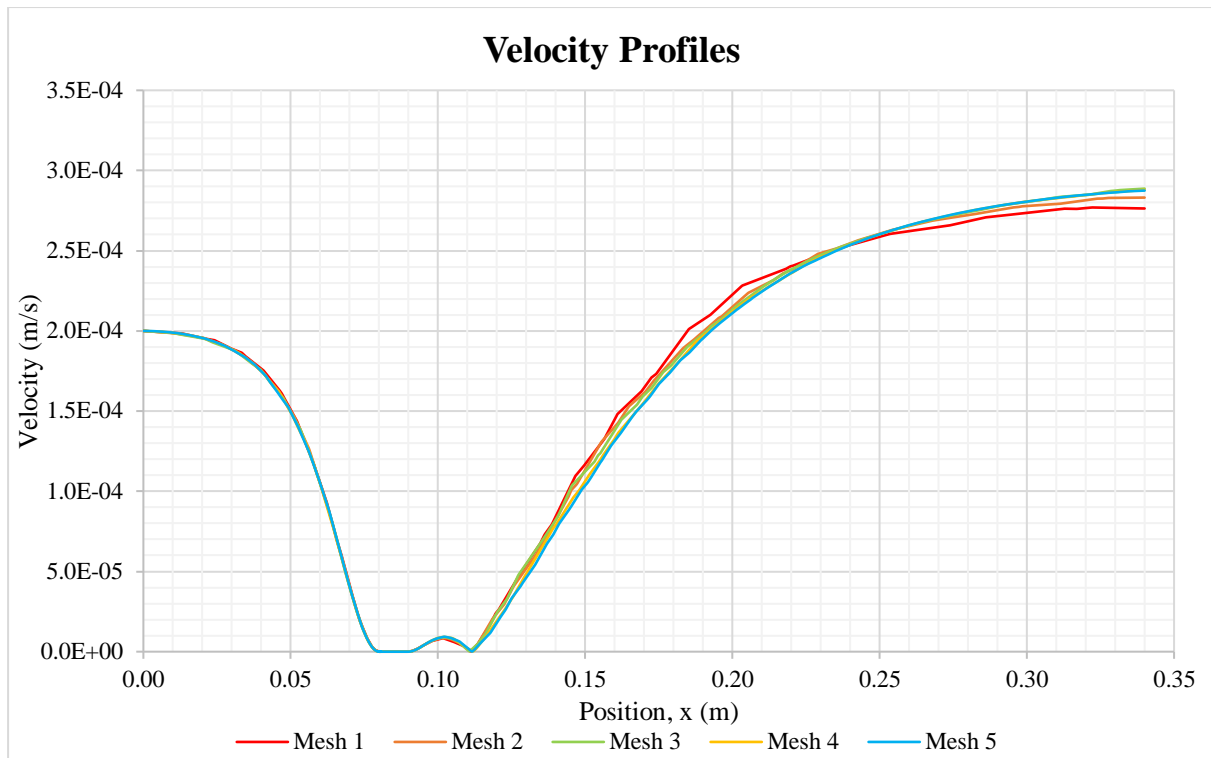| Mesh	Method	Element Size / Face Size (mm)	No. of Divisions	No. of Elements 2	Drag Coefficient	Formation Length (m)	Difference (%)	CPU Time
1 (Coarse)	Triangles	0.02	30	2799	8.3876	0.11163		0.235 sec
2 (Medium)	Triangles	0.013	48	4212	8.4568	0.11129	0.00034	0.274 sec
3 (Fine)	Triangles	0.009	77	6334	8.5107	0.11095	0.00034	0.425 sec
4 (Very Fine)	Triangles	0.006	123	10580	8.5591	0.11231	-0.00136	0.734 sec
5 (Ultra Fine)	Triangles	0.004	197	18700	8.5746	0.11197	0.00034	2.930 sec

Table 1.4(i): Mesh Refinement Table of Values

[ ] - Converged Mesh

Velocity Contour Plots

The series of velocity contour plots retrieved across the five mesh refinement stages present valuable insights into the flow behaviour around the bluff body, including flow separation, the wake region, stagnation points, and overall velocity distribution throughout the system. A constant number of contour lines (300) was employed cross all meshes to maintain consistency in visual comparison. As mesh refinement progresses from coarse (Mesh 1) to ultra-fine (Mesh 5), the contour plots show visible improvement in the clarity and detail of the velocity flow

field. Critical sections, including the areas directly upstream and downstream of the bluff body - and especially the separation region - are more defined in the contour plots of the refined meshes. For instance, a visible difference can be observed in the extent of the high-velocity area around the body during flow separation, with this area extending further downstream as mesh refinement progresses.

Velocity Profile at line A and B

The velocity profiles at Line A and Line B, as shown in Figure 1.3.2(i), illustrate velocity changes for each of the five meshes, from the rear end of the bluff body to the start of the wake region. These profiles demonstrate how mesh refinement affects the accuracy of capturing flow characteristics around the bluff body. The profiles for more refined meshes exhibit smoother, continuous lines, while the coarse meshes show slight discontinuities in velocity values toward Line B. This attests to the crucial increased accuracy that accompanies mesh refinement.

Increasing Number of Mesh Elements Vs Drag Coefficient

As seen in Table 1.3.3(i), drag coefficient values are comparatively lower in coarser meshes, with mesh 1 yielding a drag coefficient of 8.3876 while mesh 5 returned 8.5746. This trend implies that finer meshes are able to better capture flow details around the bluff body resulting in more accurate estimation of drag forces. Additionally, the increasing drag coefficient with mesh refinement which appears to stabilise after Mesh 4 as shown in Figure 1.3.3(i), indicates convergence. This highlights the effectiveness of the mesh refinement in improving accuracy up to an optimal point.

Formation Length and Velocity Profiles at each Mesh Size.

The formation length is the distance from the rear end of the bluff body to the point where velocity begins to pick up again. As shown in Table 1.3.4(i), the formation length exhibits only slight fluctuations across the five meshes, suggesting that the overall flow recovery trend remains relatively stable. Although these changes are small, Mesh 4 and Mesh 5 exhibit slight increase in formation length, indicating that finer meshes may capture subtle flow features that influence wake length.

The velocity profiles for all meshes have been plotted on the same set of axes (see Figure 1.3.4(i)) to better visualise differences brought about by mesh refinement in terms of velocity variation along the domain length. One key observation that can be made from this graph is the

difference in smoothness of the plots, wherein the coarse meshes (Meshes 1 & 2) produced profiles with more staggered curves unlike the refined mesh (Mesh 5) which produced a smoother flowing velocity profile. This is due to the increasing number of nodes that accompany with each mesh refinement stage. This leads to more discrete points allowing for more accurate estimation of the exact velocity, thus resulting in a smoother more defined velocity profile.

Grid Size Selection

By examining convergence in drag coefficient and formation length as well as computational efficiency, the mesh refinement study provides a strong foundation for selecting the appropriate grid size. As mesh resolution increases from Mesh 1 (Coarse) to Mesh 5 (Ultra Fine) the drag coefficient and formation length values stabilize, showing minimal changes between finer meshes (Mesh 4 and Mesh 5). This convergence indicates that further refinement will produce limited accuracy improvement with the penalty of increasing computational time.

Mesh 4 ("Very Fine") demonstrates an optimal balance between computational time and accuracy in results. This accuracy can be seen in the 1.55% difference in drag coefficient values between Mesh 4 ($C_D = 8.5591$) and Mesh 5 ($C_D = 8.5746$), and a similar closeness in formation length values. Thus Mesh 4 is identified as the converged mesh for this analysis, making it the optimal grid size for balancing accuracy and efficiency in this study.

2 PART 2: RESULTS AND DISCUSSION

2.1 2D STEADY CASES AT $\alpha = 0°$ FOR NACA0012 & NACA4412

2.1.1 Drag Coefficient & Lift Coefficient Validation – NACA0012 Model [1 Mark]

Reference Values		
Drag Coefficient (C_D)	$C_D \approx 0.009$	
Lift Coefficient (C_L)	$C_L \approx 0$	
Validated Values		% Error
Drag Coefficient (C_D)	$C_D \approx 0.009$	0%
Lift Coefficient (C_L)	$C_L \approx 0$	0%

Table 2.1.1(i): Table of Reference and Validated Values for C_D & C_L (NACA0012)

```
    lift-coefficient
    ------------------
                                    Cl
    -------------------------------- --------------------
         wall-part-surface_body        -0.0011347996

    drag-coefficient
    ------------------
                                    Cd
    -------------------------------- --------------------
         wall-part-surface_body         0.0092461746
```

Figure 2.1.1(i): ANSYS Output of Reference and Validated Values for C_D & C_L (NACA0012)

2.1.2   Drag Coefficient & Lift Coefficient Validation – NACA4412 Model [1 Mark]

Reference Values		
Drag Coefficient (C_D)	$C_D \approx 0.01$	
Lift Coefficient (C_L)	$C_L \approx 0.41$	
Validated Values		Percentage error
Drag Coefficient (C_D)	$C_D \approx 0.01$	0%
Lift Coefficient (C_L)	$C_L \approx 0.44$	7%

Table 2.1.2(i): Table of Reference and Validated Values for C_D & C_L (NACA4412)

```
          lift-co
    ------------------
                                    Cl
    -------------------------------- --------------------
         wall-part-surface_body         0.43723958

          drag-co
    ------------------
                                    Cd
    -------------------------------- --------------------
         wall-part-surface_body         0.010213656
```

Figure 2.1.2(i): ANSYS Output of Reference and Validated Values for C_D & C_L (NACA4412)

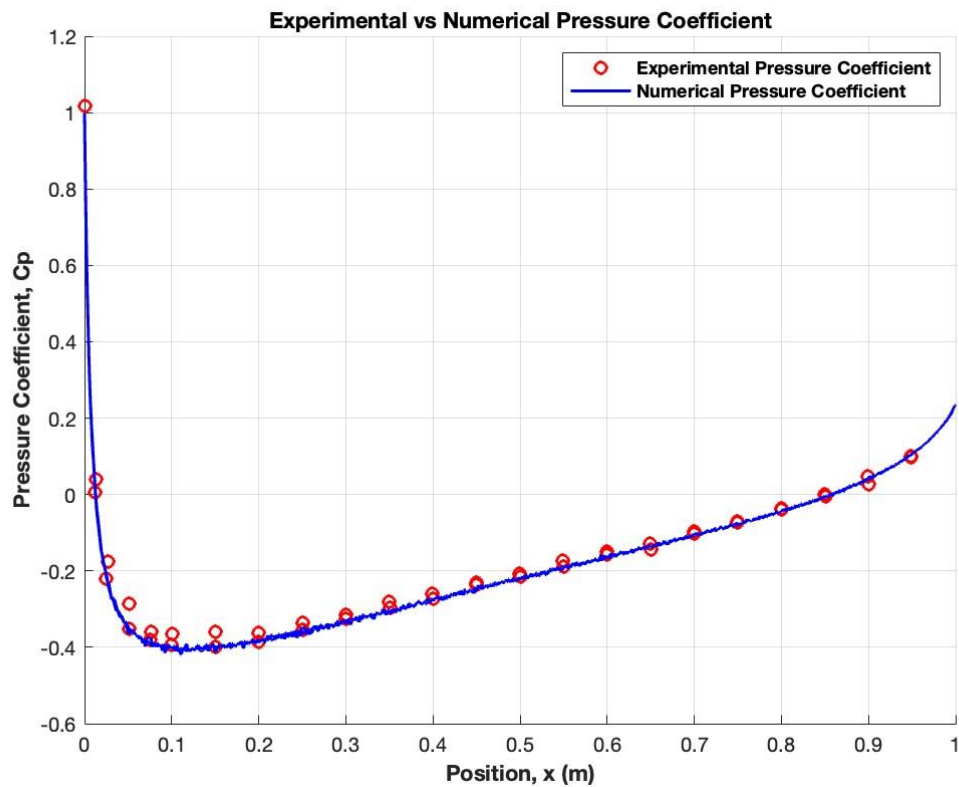### 2.1.3 Pressure Coefficient Validation [1 Mark]

Figure 2.1.3(i): Experiment vs. Numerical Pressure Coefficient Plot for NACA0012 Model

2.1.4 Table of Pressure Difference, Pressure Drag Force, & Skin-Friction (Viscous) Drag Force [2 Mark]

	NACA 4412	NACA 0012
Pressure Drag Force (N)	14.37445	9.9312646
Skin-Friction Drag Force (N)	33.679789	33.57107
Max Pressure (Pa)	4714.45	4702.82
Min Pressure (Pa)	-3483.77	-1991.21
Pressure Difference (Pa)	8198.22	6694.03

Table 2.1.4(i): Table of Pressure Difference, Pressure Drag Force, & Skin-Friction (Viscous) Drag Force

2.1.5 Pressure Contour & Velocity Streamline for NACA0012 & NACA4412 [2 Mark]
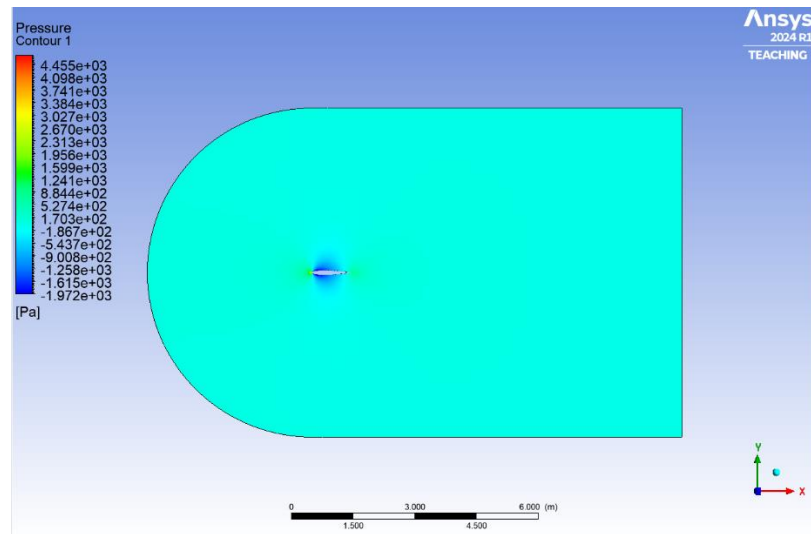

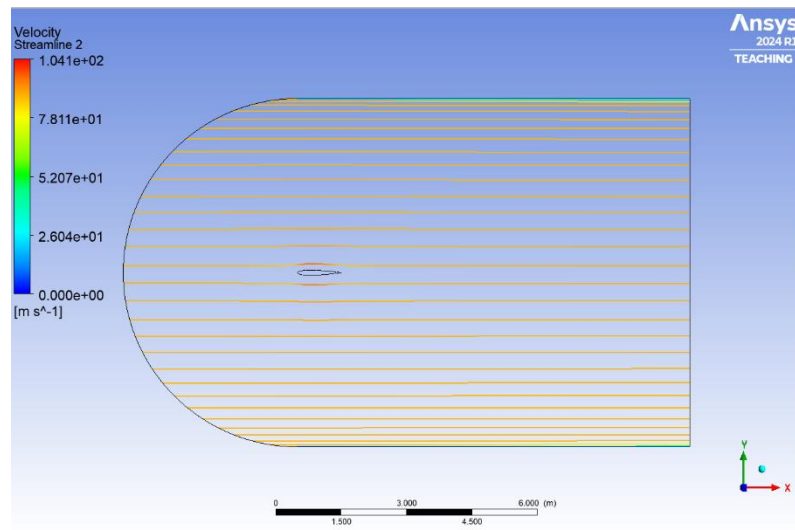Figure 2.1.5(i): Pressure Contour for NACA0012 Model at α = 0°
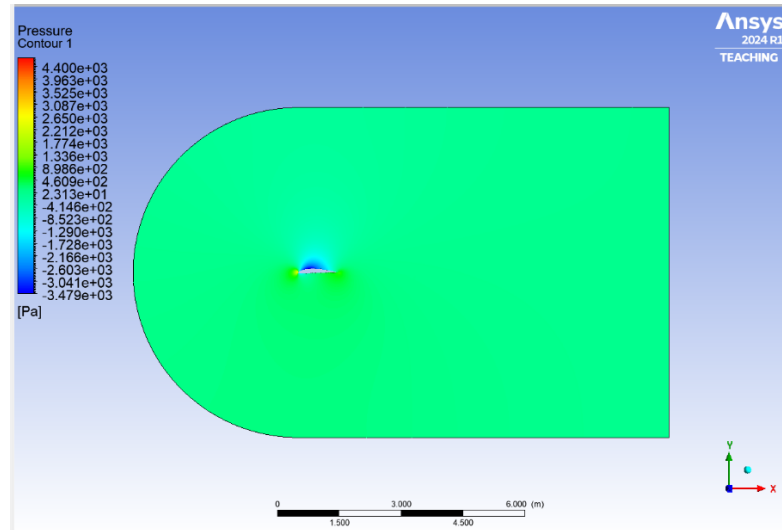

Figure 2.1.5(ii): Velocity Streamline for NACA0012 Model at α = 0°

Figure 2.1.5(iii): Pressure Contour for NACA4412 Model at α = 0°
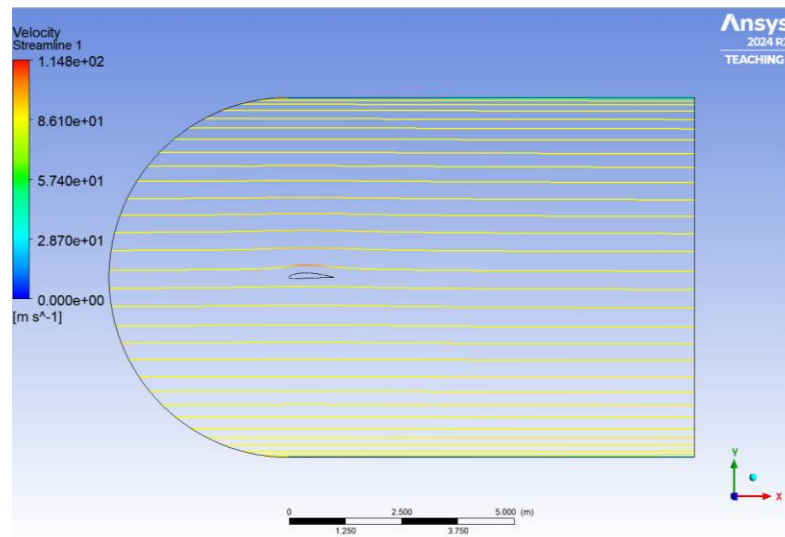

Figure 2.1.5(iv): Velocity Streamline for NACA4412 Model at α = 0°

2.1.6 Discussion on the Lift for the NACA0012 Model [1 Mark]

For the NACA0012 aerofoil at $\alpha = 0°$, there is no lift being produced since the aerofoil at this stage is symmetrical. The NACA0012 aerofoil itself, presents in a completely symmetrical state unlike NACA4412. When the angle of attack is 0°, the airflow travels over both of the surfaces in the same way, creating an equal pressure distribution on the top and bottom surfaces. Since there are no pressure differences that would cause the aerofoil to rise, net lift is not generated from the aerofoil.

The above scenario ($C_L \approx 0$) is consistent with theoretical predictions for symmetrical aerofoils since the lift coefficient verifies that there is no lift force operating on the aerofoil at zero angle of attack. Since lift is generated by pressure differences, a lack of camber and a zero angle of attack mean that the necessary conditions for lift are not present [4].

2.1.7   Discussion on the Lift for the NACA4412 Model [1 Mark]

The NACA4412 aerofoils generates lift at $\alpha = 0°$, due to its asymmetrical (cambered) shape. The NACA4412 aerofoil has a flat lower surface and a curved top surface, in contrast to the symmetrical NACA0012. The airflow route is altered by this camber, moving more slowly beneath the flat lower surface and more quickly over the curved upper surface. Bernoulli's principle states that air flowing more slowly produces higher pressure and air travelling more quickly produces lower pressure. Thus, an upward force, lift, is produced by this pressure difference – lower pressure on the top surface and higher pressure at the bottom. As seen in the results above, the lift coefficient is ($C_L \approx 0.44$), for the NACA4412 model, confirming that lift is being generated even at a low angle of attack. This is consistent with aerodynamic theory for cambered aerofoils, where the curvature enables lift production without requiring a high angle of attack [1].

The following figures are visual illustrations of the shapes of the NACA0012 and NACA4412 aerofoils. The NACA0012 is a symmetrical aerofoil with no camber, while the NACA4412 is cambered, resulting in an asymmetrical profile that enables it to generate lift even at zero angle of attack.
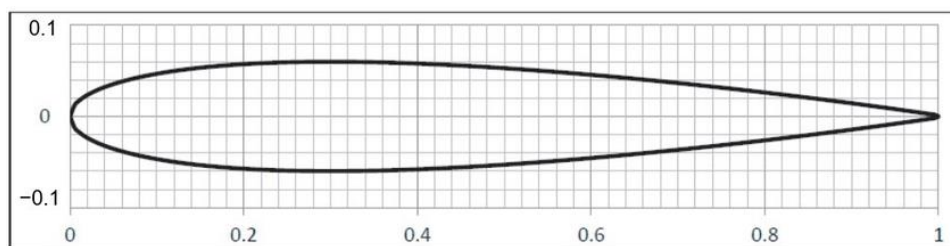

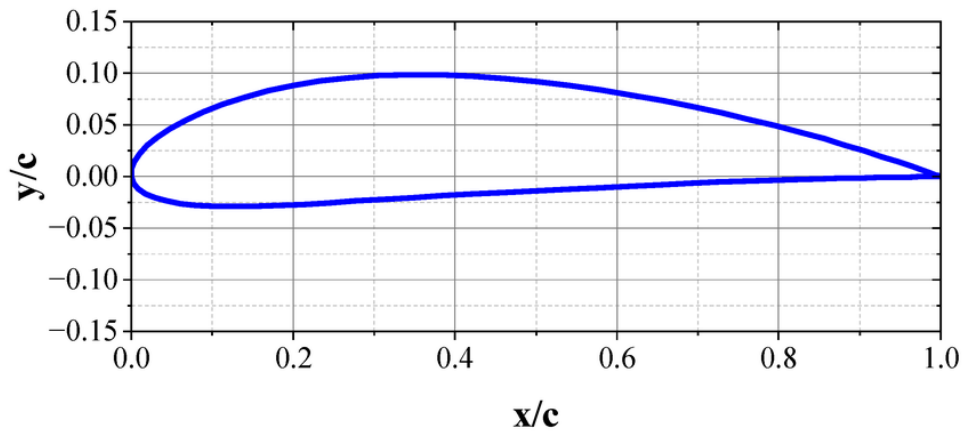Figure 2.1.7(i): Profile of NACA0012 Aerofoil (Symmetrical Design) [1]

Figure 2.1.7(ii): Profile for NACA4412 Aerofoil (Symmetrical Design) [1]

2.2 2D STEADY CASES AT α = 5°, 10°, 15° FOR NACA4412

2.2.1 Drag Coefficient & Lift Coefficient [1 Mark]

Angle of Attack (α)	Drag Coefficient, C_D	Lift Coefficient, C_L
5°	0.014943427	0.98251979
10°	0.02592154	1.472477
15°	0.039009861	1.8181889

Table 2.2.1(i): Table of Values for Drag Coefficient & Lift Coefficient

2.2.2 Table of Pressure Difference, Pressure Drag Force, & Skin-Friction (Viscous) Drag Force [1 Mark]

Angle of Attack (α)	Pressure Drag Force (N)	Skin-Friction Drag Force (N)	Pressure Difference (Pa)
5°	36.303181	34.004163	11708.66
10°	89.617405	32.340872	25089.67
15°	154.20662	29.330905	44884.12

Table 2.2.2(i): Table of Values for Pressure Difference, Pressure Drag Force, & Skin-Friction (Viscous) Drag Force

2.2.3 Pressure Contour & Velocity Streamline for all cases [2 Marks]
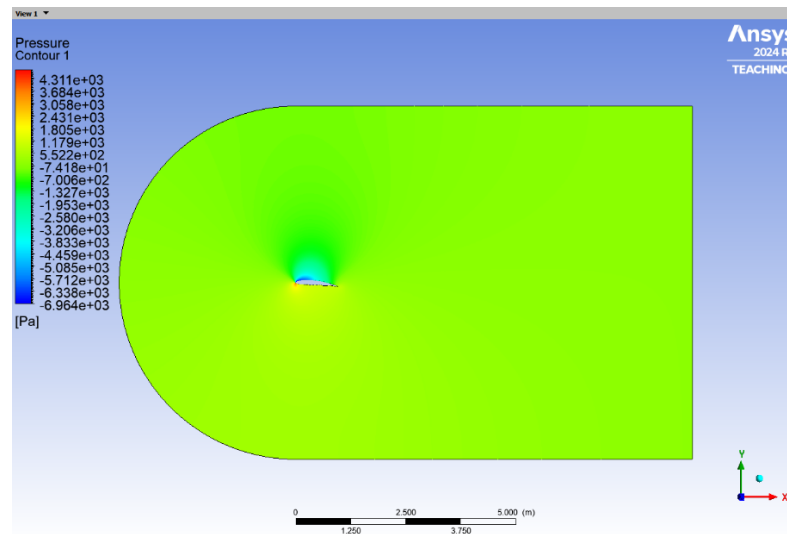

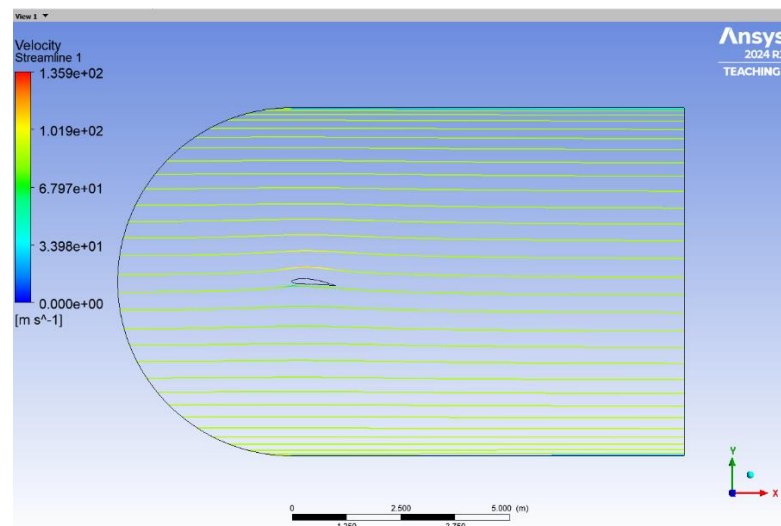Figure 2.2.3(i): Pressure Contour for NACA4412 Model at α = 5°
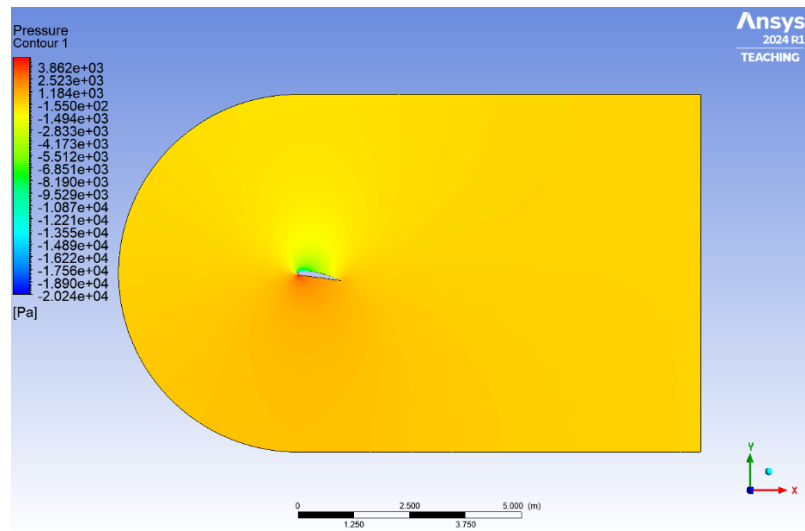

Figure 2.2.3(ii): Velocity Streamline for NACA4412 Model at α = 5°
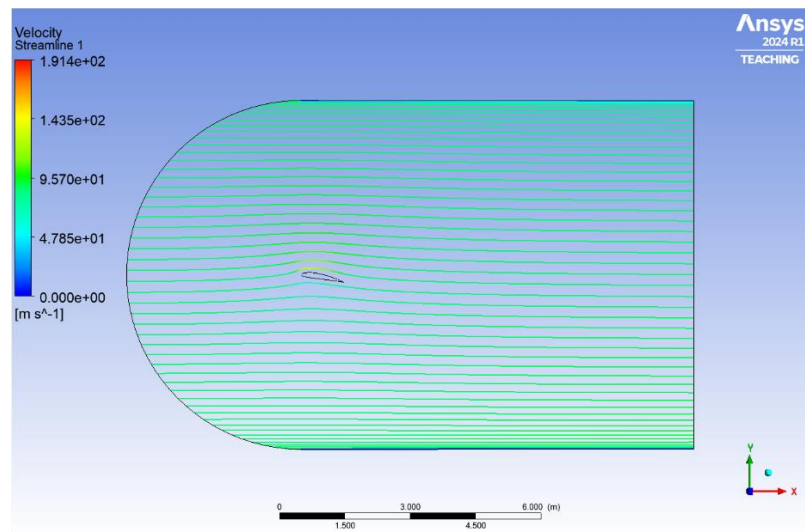
Figure 2.2.3(iii): Pressure Contour for NACA4412 Model at α = 10°
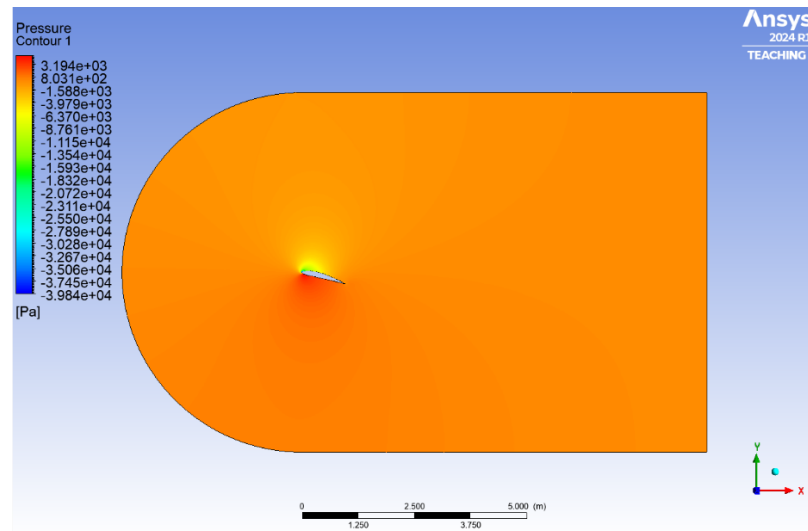

Figure 2.2.3(iv): Velocity Streamline for NACA4412 Model at α = 10°

Figure 2.2.3(v): Pressure Contour for NACA4412 Model at α = 15°

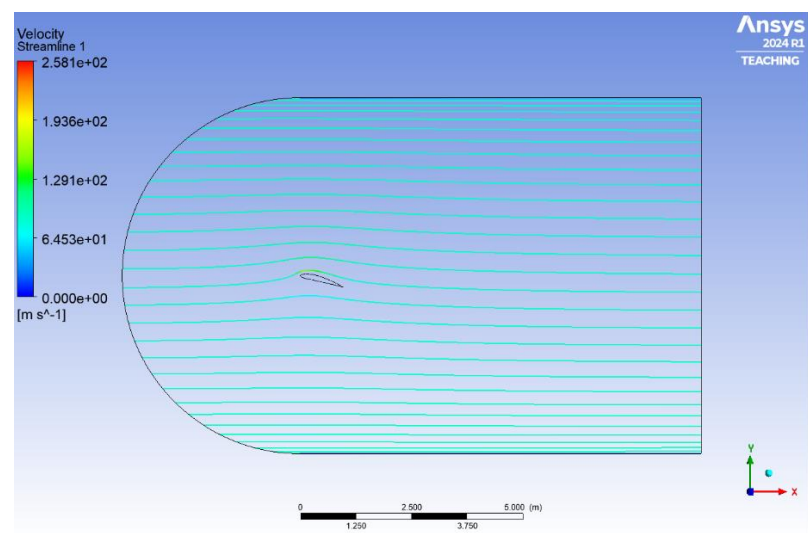Figure 2.2.3(vi): Velocity Streamline for NACA4412 Model at α = 15°

2.3 2D TRANSIENT CASE AT α = 20° FOR NACA4412

2.3.1 Average Drag Coefficient (C_D) & Average Lift Coefficient (C_L) [1 Mark]

NACA 4412 at $\alpha = 20°$	
Average Drag Coefficient (C_D)	0.190869
Average Lift Coefficient (C_L)	1.425064

Table 2.3.1(i): Table of Values for Average Drag & Lift Coefficient

Note: Average Lift and Drag Coefficients were calculated using values within the steady state region. Refer to Figure 3.3.1(ii) and Figure 3.3.1(iv)
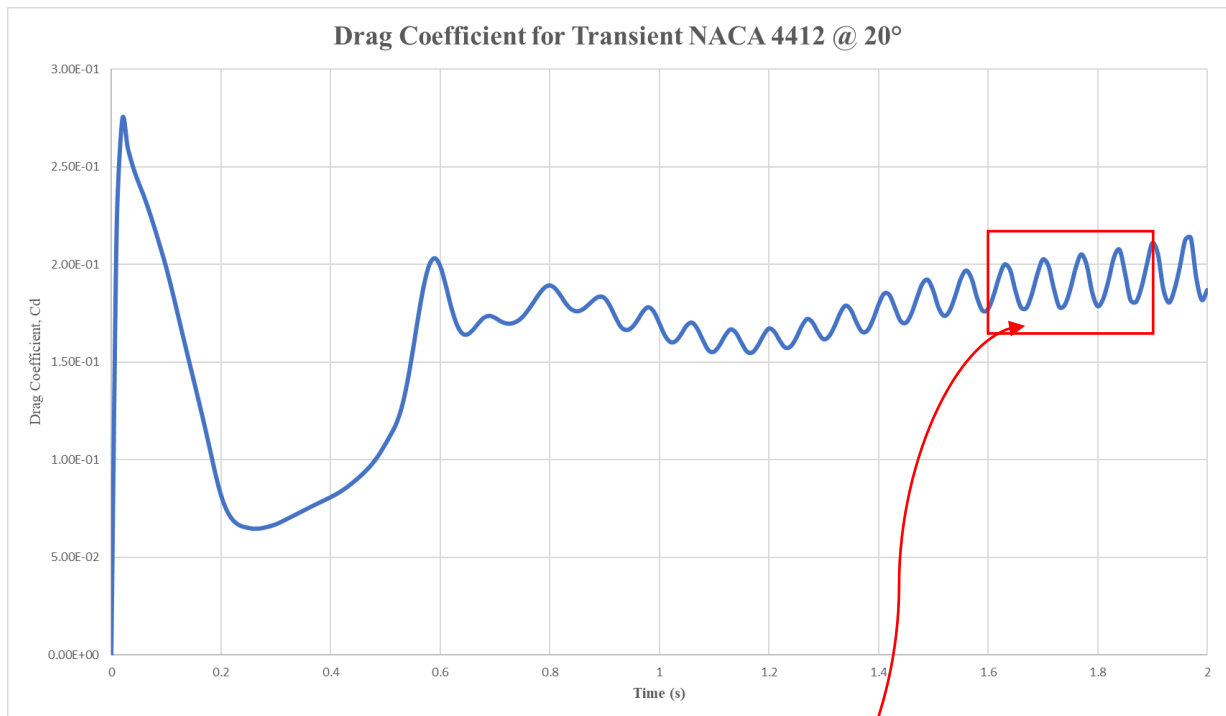
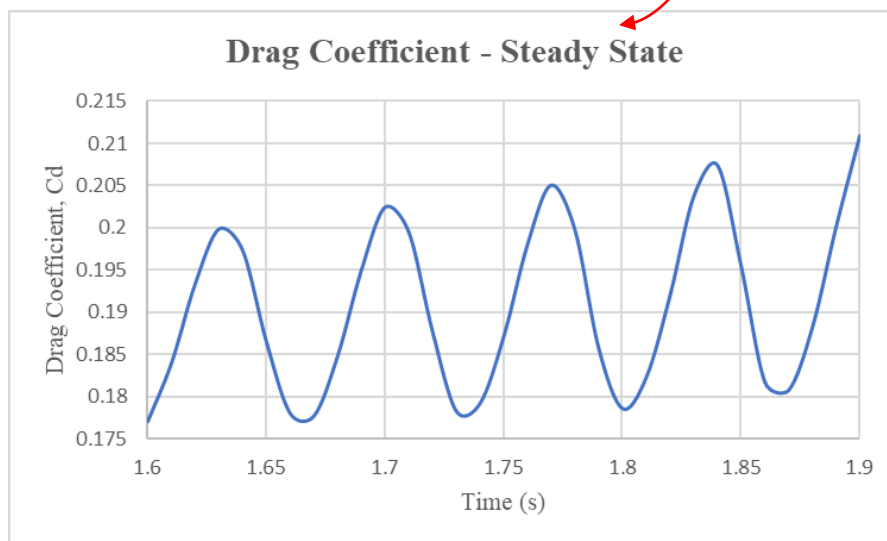Figure 2.3.1(i): Plot of Drag Coefficient vs. Time for NACA4412 at α = 20° (Entire Graph)

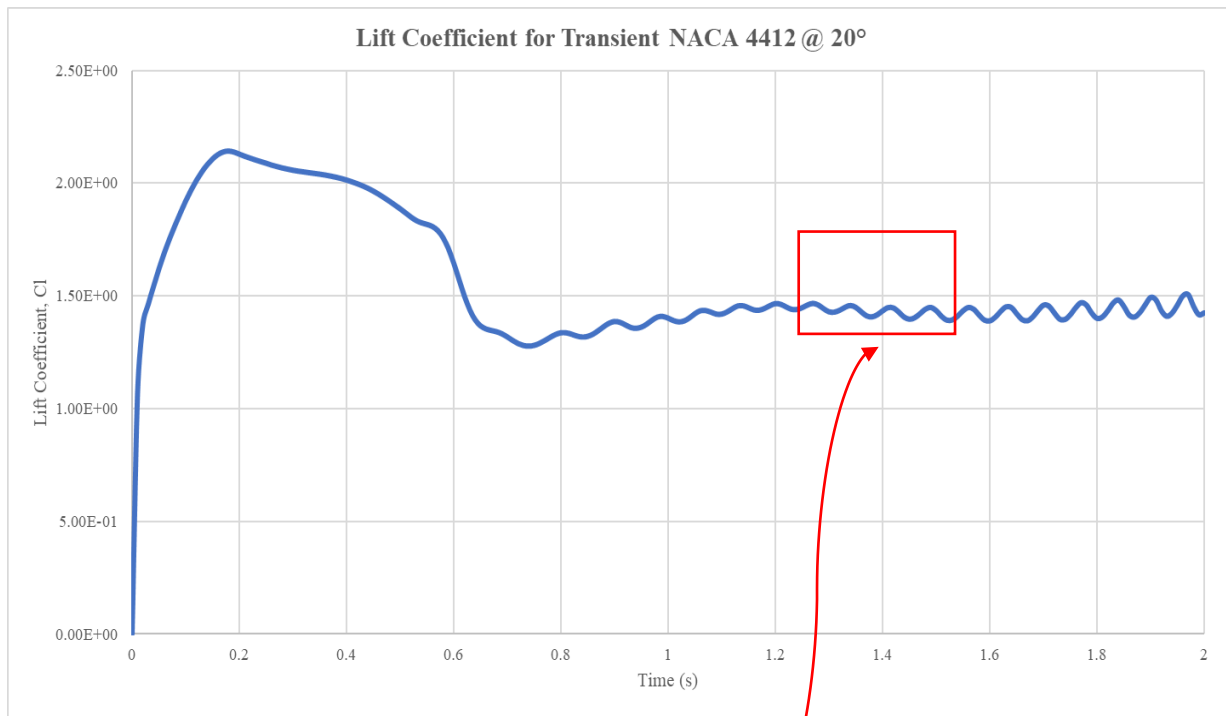Figure 2.3.1(ii): Plot of Drag Coefficient vs. Time for NACA4412 at α = 20° (Selected Steady Section of the Graph)

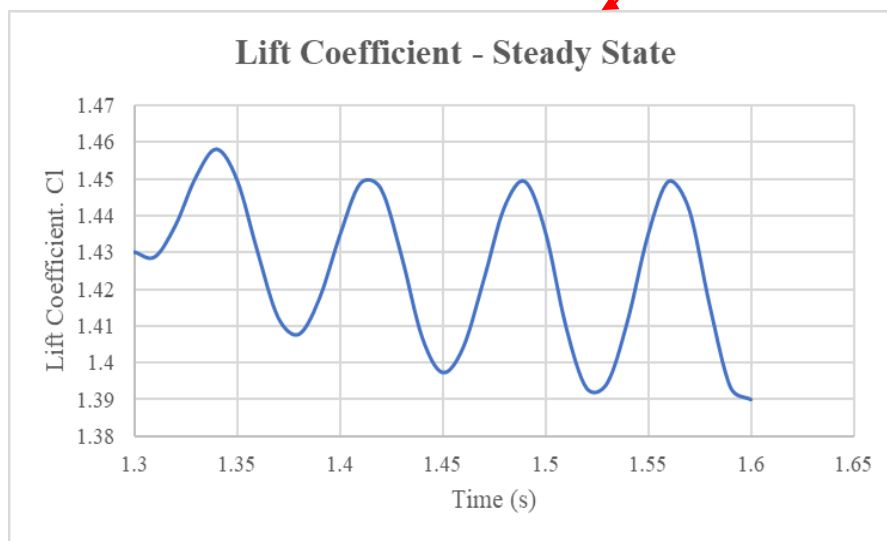Figure 2.3.1(iii): Plot of Lift Coefficient vs. Time for NACA4412 at α = 20° (Entire Graph)

Figure 2.3.1(iv): Plot of Lift Coefficient vs. Time for NACA4412 at α = 20° (Selected Steady Section

of the Graph)

2.3.2 Table of Pressure Difference, Pressure Drag Force, & Skin-Friction (Viscous) Drag Force [1 Mark]

Pressure Drag Force (N)	862.20804
Skin-Friction Drag Force (N)	16.536908
Max Pressure (Pa)	4803.49
Min Pressure (Pa)	-35825.4
Pressure Difference (Pa)	40628.89

Table 2.3.2(i): Table of Values for Pressure Difference, Pressure Drag Force, & Skin-Friction (Viscous) Drag

2.3.3 Pressure Contour & Velocity Streamline Plots at T=2sec [1 Mark]
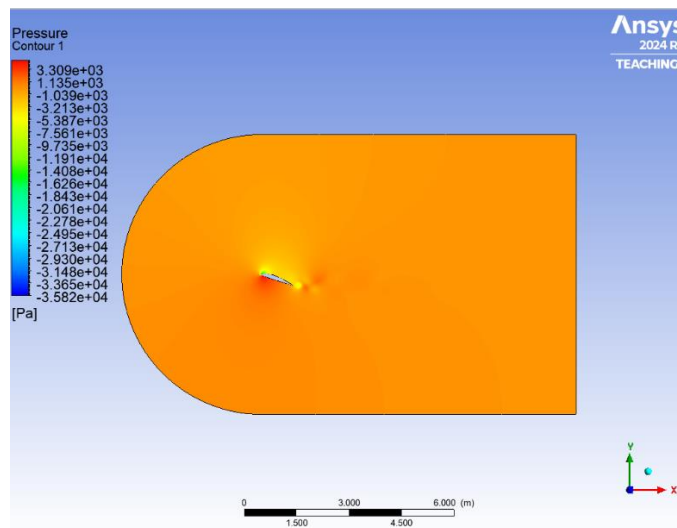
Figure 2.3.3(i): Plot for Pressure Contour at T=2sec for NACA4412 at α = 20° for Transient Flow
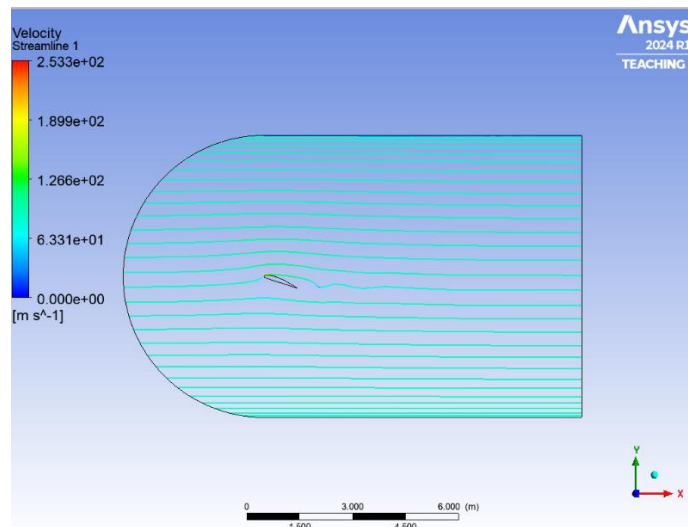
Figure 2.3.3(ii): Plot for Velocity Streamline at T=2sec for NACA4412 at α = 20° for Transient Flow

2.3.4   Strouhal Number Results & Discussion on Mild Vortex Shedding at α = 20° [2 Marks]

The Strouhal Number for the NACA4412 aerofoil at an angle of attack of 20° was calculated to understand the occurrence of mild vortex shedding.

$Characteristic\ Length\ (L) = 1\ metre$

$Characteristic\ Velocity\ (U) = 87.644\ \frac{metre}{second}$

Figure 2.3.4(i): Indicating Period Values in Lift Coefficient vs. Time Plot for Transient Flow at α = 20°

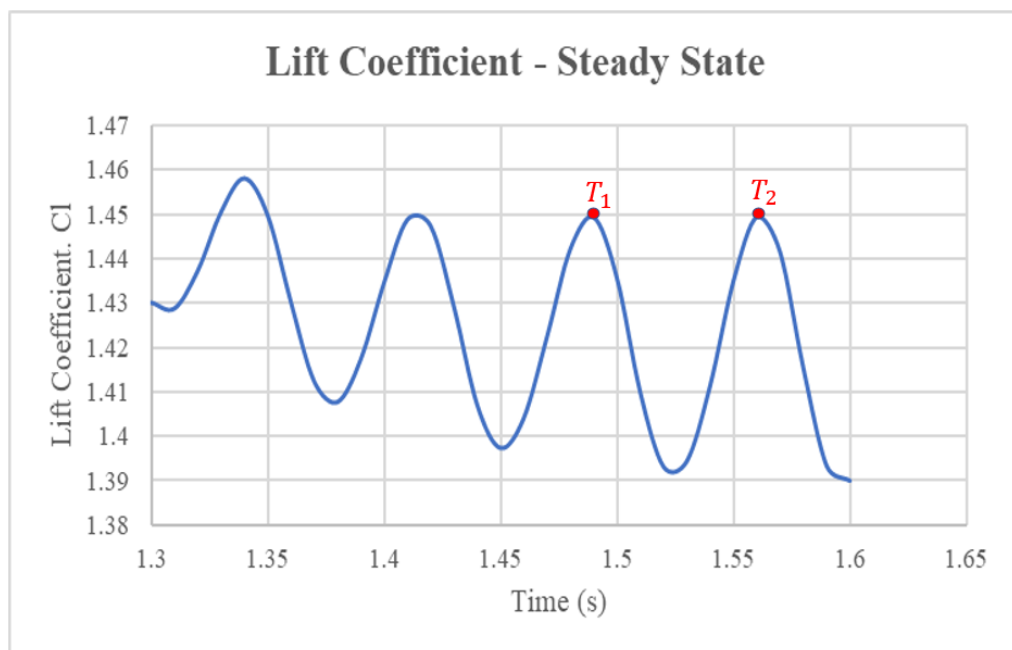$Period\ (T) = T_2 - T_1 = 1.56 - 1.48 = 0.08\ seconds$ (Rounded up to second decimal)

$frequency\ (f) = \frac{1}{0.08} = 12.5\ Hertz$

$$St = \frac{f.L}{U}$$

Where, f = shedding frequency, L = characteristic length, U = characteristic velocity

$St = \frac{f.L}{U} = \frac{12.5*1}{87.644} = 0.1426$ (Inertial Effects Dominate)

The Strouhal number at α=20° indicates that the aerofoil has minor vortex shedding, which is normal for vortex shedding over bluff bodies (usually between 0.1 and 0.3) [2][8]. Mild vortex shedding implies that small-scale vortices are shed from the trailing edge as a result of periodic, mild separation and reattachment of the flow surrounding the aerofoil. This behaviour is prevalent at moderate to high angles of attack, where flow separation rises but severe turbulence does not yet occur.

According to Sunden (2011) and Fu (2018), vortex shedding at specific Strouhal numbers suggests that alternating low-pressure regions form behind the aerofoil, which influences the lift and drag characteristics [2][8]. The aerofoil experiences regulated, periodic shedding rather than intense turbulence at this moderate Strouhal number, which may have an impact on lift control and stability at this angle.

2.4 2D STEADY AND TRANSIENT CASES FOR NACA4412 AEROFOIL

Note: Although the question title mentions both steady and transient 2D cases, the boundary conditions provided were not sufficient to perform transient flow simulations for $\boldsymbol{\alpha} = \boldsymbol{0}°, \boldsymbol{5}°, \boldsymbol{10}°, \boldsymbol{15}°$. The conditions specified only support transient simulation for α=20°. Additionally, it was explicitly stated in the requirements: "A 2D transient simulation is required only for the case α=20°."

2.4.1 Plot & Discussion for C_D vs. α (for all α cases) [1 Mark]
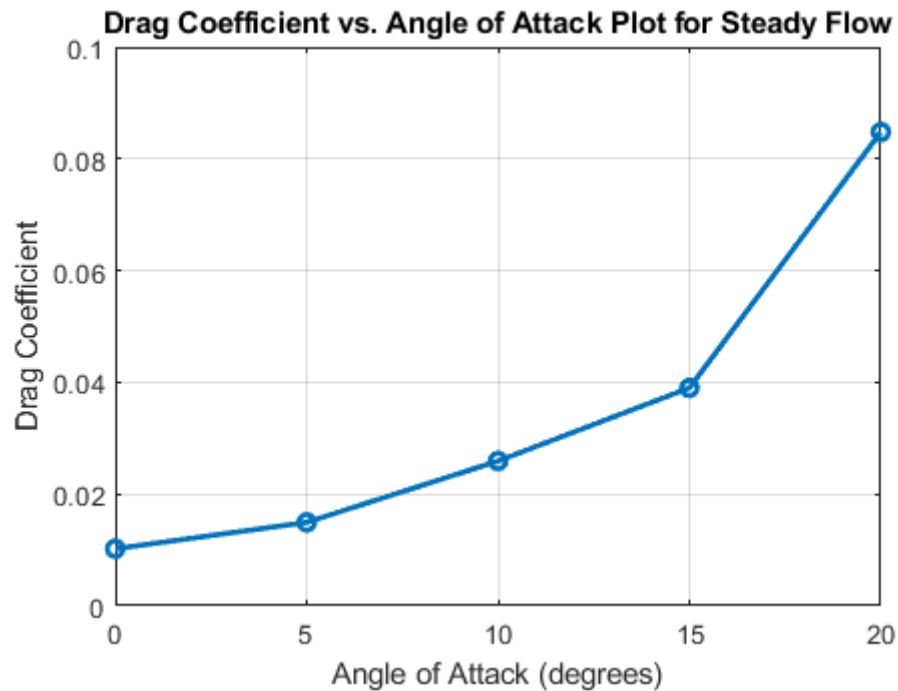

Figure 2.4.1(i): Plot for Drag Coefficient (C_D) vs. Angle of Attack (α) for Steady Flow

The trend observed in the drag coefficient (C_D) vs angle of attack (α) plot aligns well with the findings in the recent research. At low angles of attack (0° and 10°), C_D gradually increases due to minimal pressure drag as the aerofoil stays aligned with the aerofoil, according to Krishnan and Roy's (2022) [4] analysis of the aerodynamic properties of NACA aerofoils. The study also displayed that as the angle of attack approaches 15° and over, the flow demonstrated a sharp rise in drag, which is attributed to increased flow separation and turbulence at these higher angles. This behaviour is properly in line with the stimulated graph, which increases significantly beyond 10°, confirming that the findings are consistent with the current research. This upward trend validates the accuracy of the simulation trends and supports the concept that higher angles result in increased resistance since the aerofoil blocks more incoming airflow, increasing the pressure drag component [4].

2.4.2   Plot & Discussion for C_L vs. α (for all α cases) [1 Mark]
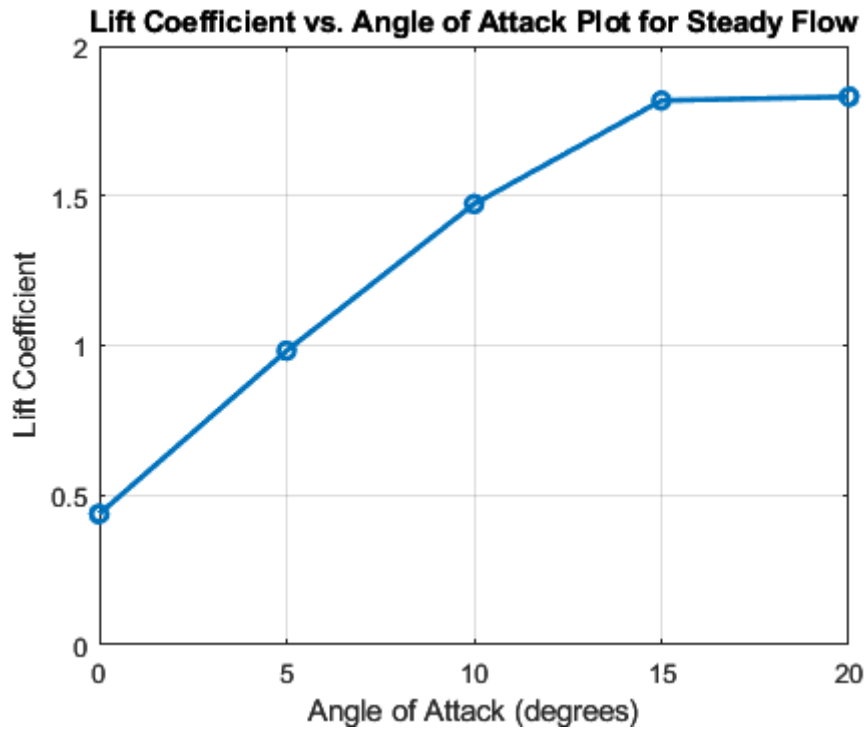

Figure 2.4.1(ii): Plot for Lift Coefficient (C_L) vs. Angle of Attack (α) for Steady Flow

The lift coefficient (C_L) vs. the angle of attack plot above demonstrated a typical lift behaviour, where C_L increases with the angle of attack up to a certain point. C_L rises steadily from 0° to 15° in this plot, indicating that lift increases as the aerofoil tilts further against the incoming wind. The C_L levels off after 15°, indicating that the aerofoil has achieved its maximum lift capacity at this angle of attack. This behaviour is consistent with the findings of Krishnan and Roy's (2022) [4], who observed similar patterns in their research of modified NACA aerofoils, with lift increasing at lower angles and levelling off as stall conditions approached. The patterns seen here are validated by the consistency of our graph with previous studies, which shows that the simulation findings accurately capture the expected aerodynamic behaviour.

2.4.3 Plot & Discussion for C_L/C_D vs. α (for all α cases) [1 Mark]
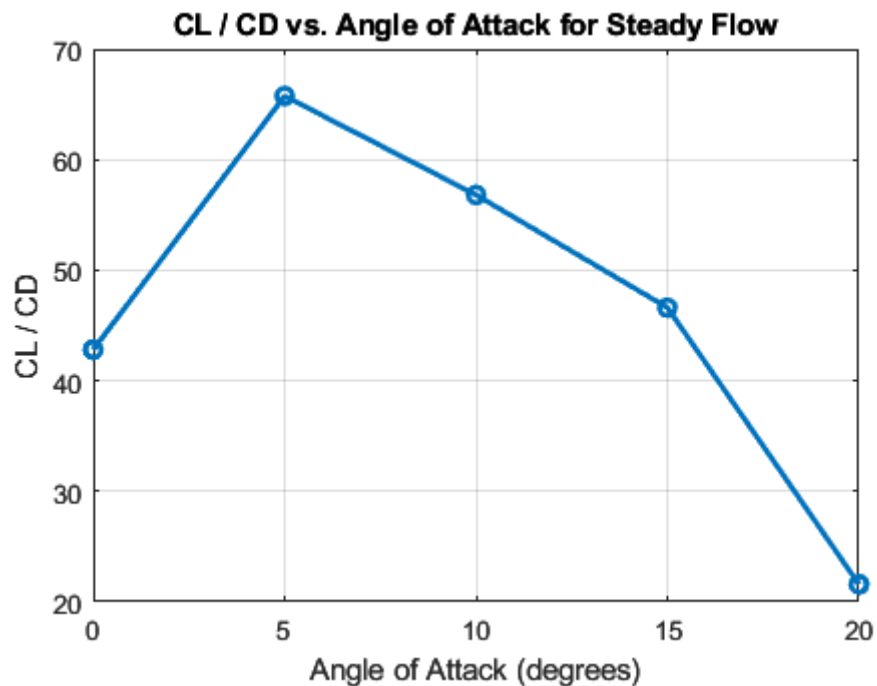

Figure 2.4.1(iii): Plot for Lift Coefficient/Drag Coefficient $(\frac{C_L}{C_D})$ vs. Angle of Attack (α) for Steady Flow

The above C_L/C_D vs. angle of attack plot revealed the aerofoil's aerodynamic efficiency at different angles. At 5°, the lift-to-drag ratio peaked indicating that the angle is the most efficient angle of attack for the NACA4412 aerofoil in terms of optimising lift and reducing drag. The ratio continued to decrease as the angle increased, revealing that at greater angles, drag begins to outweigh the benefits of additional lift. This pattern is consistent with research from airfoiltools.com [5], which found that the NACA4412 aerofoil's polar curves exhibit a peak in aerodynamic efficiency at low angles, followed by a decrease when drag increases more rapidly relative to lift.

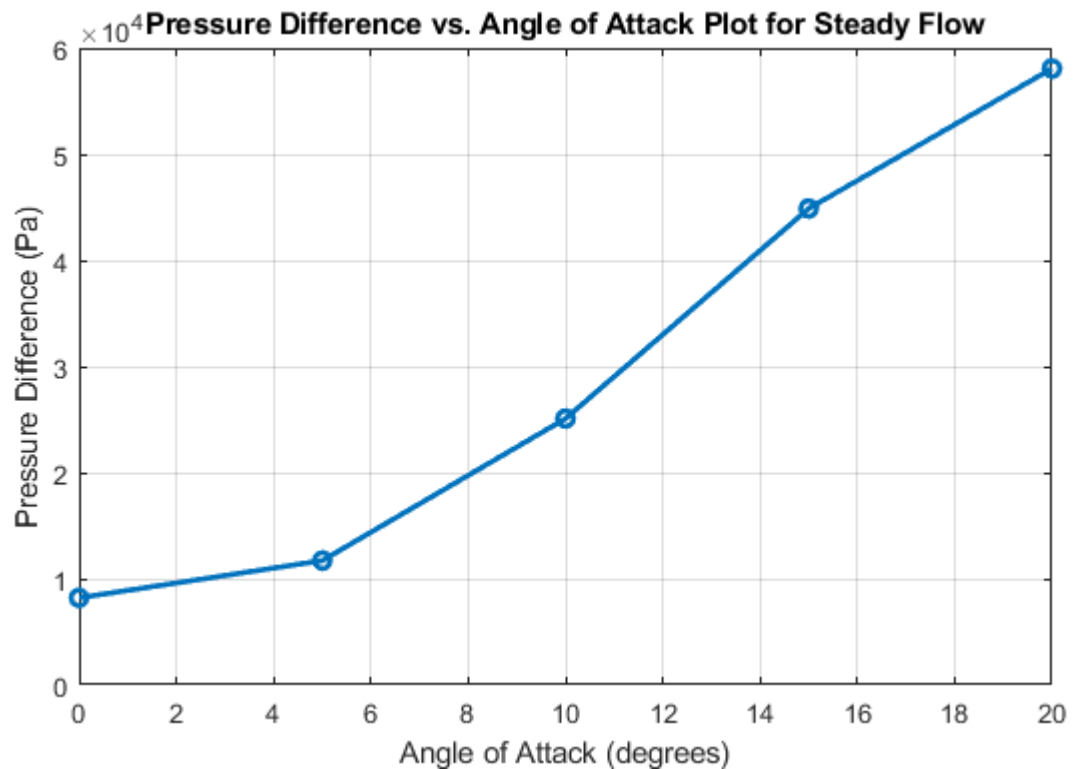2.4.4   Plot & Discussion for Pressure Difference vs. α (for all α cases) [1 Mark]

Figure 2.4.1(iv): Plot for Pressure Difference vs. Angle of Attack (α) for Steady Flow

The pressure difference vs. angle of attack plot displayed clear upward trend in pressure difference as the angle increases. As the aerofoil tilts more into the airflow, a larger pressure differential forms between the upper and lower surfaces, which is a key component in generation lift-thus, explaining an increase in the plot. At low angles, 0° to 10°, the pressure only increases gradually, whereas beyond 10°, the increase becomes steeper, suggesting a stronger lift generation as the aerofoil reaches higher angles of attack. This trend continues up to 20°, where the pressure difference reaches its peak, demonstrating the aerofoil can generate under steady flow conditions. The gradual increase in pressure differential with angle is consistent with theoretical assumptions, proving the aerofoil's ability to generate more lift at increasing angles until it reaches its aerodynamic limits.

2.4.5   Plot & Discussion for Skin-Friction Drag and Pressure Drag vs. α (for all α cases) & Approximation of the Intersection Point [1 Mark]
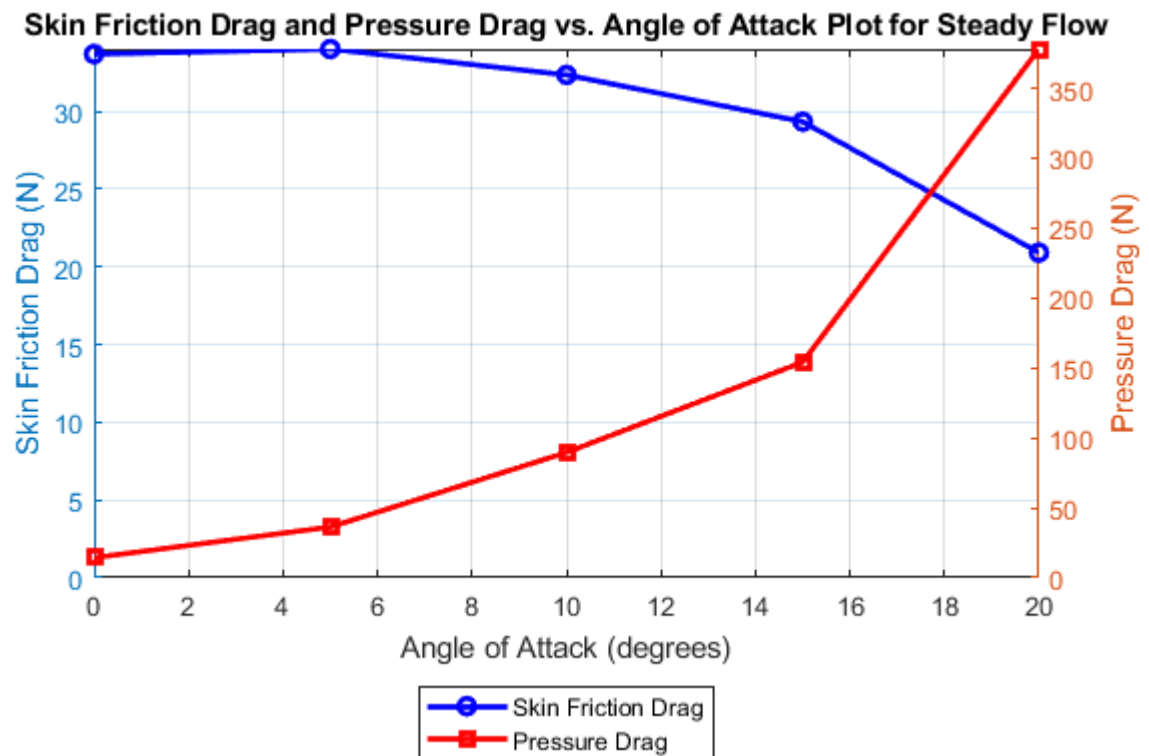

Figure 2.4.5(v): Plot for Skin-Friction Drag and Pressure Drag vs. Angle of Attack (α) for Steady Flow

The skin-friction drag and pressure drag vs. angle of attack plot illustrates distinct behaviours of these two drag components under varying angles. As the angle increases, pressure drag increases significantly, particularly above 10°, due to increased resistance as the aerofoil directly faces more of the incoming airflow. Skin-friction drag, on the other hand, only slightly decreases at greater angles and is comparatively constant. The mentioned pattern aligns with research showing that surface properties, not angle of attack, are the main factors influencing skin-friction drag [7]. Around 17°, the two drag components overlap, signifying a critical moment at which pressure drag takes over as the predominant drag type. This shift emphasizes the aerofoil's transition at high angles, where flow separation and turbulence significantly increase the pressure drag relative to skin-friction drag.

2.4.6   Discussion in a Scenario involving an Aeroplane

2.4.6.1 What angle of attack (α) is most optimal during take-off, and why? [1 Mark]

The most optimal angle of attack for take-off would be at 15°. According to the results from the NACA4412 aerofoil, the lift coefficient (C_L) significantly increases at this angle, providing the lift

required to overcome the aircraft's weight and start the flight. [4]. The drag coefficient (C_D) at 15° is still mild, as shown in Figure 2.4.1(i), enabling the plane to generate enough lift without experiencing excessive drag. Memon (2023) [6], stated that a smooth ascent depends on achieving a balance between lift and drag during take-off, and the C_L vs. α plot in Figure 2.4.1(ii) shows that 15° achieves this balance effectively, aligning with practical take-off dynamics by reaching high lift levels without a sharp rise in drag.

2.4.6.2 What angle of attack (α) is most efficient during cruise control conditions, and why? [1 Mark]

For cruise control, the most efficient angle of attack is at 5°. As shown in Figure 3.4.1(iii), the lift-to-drag ratio (C_L/C_D) peaks at this angle, which makes it perfect for level, effective flight with minimal drag [3]. Maintaining a low angle of attack, and keeping level during cruising conditions enables the aircraft to fly more economically since increased efficiency lowers the total drag force relative to lift [3]. This is supported by the trend in the C_L/C_D plot, which showed a peak in aerodynamic efficiency at low angles, confirming that the ideal range for cruise circumstances is at 5°.

3 REFERENCE

[1]   V. Akbari, M. Naghashzadegan, R. Kouhikamali, F. Afsharpanah, and W. Yaïci, "Multi-Objective Optimization of a Small Horizontal-Axis Wind Turbine Blade for Generating the Maximum Startup Torque at Low Wind Speeds," *Machines*, vol. 10, no. 9, p. 785, Sep. 2022, doi: https://doi.org/10.3390/machines10090785.

[2]   F. Fu, "Vortex Shedding - an overview | ScienceDirect Topics," www.sciencedirect.com, 2018. Available: https://www.sciencedirect.com/topics/engineering/vortex-shedding

[3]   "How Do Planes Take Off? The Science Behind The Flight | News," Flydays, 2023. Available: https://www.flydays.co.uk/news/how-do-planes-take-off-the-science-behind-the-flight/

[4]   A. Krishnan and S. Roy, "Aerodynamic Profile Modification of a NACA 0012 Aerofoil for Enhanced Lift-Drag Characteristics at Low Reynolds Number," *U.Porto Journal of Engineering*, vol. 8, no. 2, pp. 156–168, Apr. 2022, doi: https://doi.org/10.24840/2183-6493_008.002_0012.

[5]   "NACA 4412 (naca4412-il) Xfoil prediction polar at RE=1,000,000 Ncrit=9," airfoiltools.com. Available: http://airfoiltools.com/polar/details?polar=xf-naca4412-il-1000000

[6]   D. O. Memon, "An Aircraft's Angle Of Attack: Everything You Need To Know," Simple Flying, Oct. 12, 2023. Available: https://simpleflying.com/angle-of-attack-complete-guide/

[7]   "Skin Friction Drag - an overview | ScienceDirect Topics," Sciencedirect.com, 2013. Available: https://www.sciencedirect.com/topics/engineering/skin-friction-drag

[8]   B. Sunden, *Vortex Shedding*. Begel House Inc., 2011. Available: https://www.thermopedia.com/content/1247/